coatings

MDPI

Article

A Study on Improving the Sensitivity of Indirect X-ray Detectors by Adding Hybrid Perovskite Quantum Dots

Kwanyong Lee [1], Jehoon Lee [1], Daeho Han [1], Hailiang Liu [1] and Jungwon Kang [1,2,*]

[1] Department of Electronic and Electrical Engineering, Dankook University, Yongin 16890, Korea; legacy35495@dankook.ac.kr (K.L.); usyj0512@gmail.com (J.L.); handae96@naver.com (D.H.); liuhailiang107@gmail.com (H.L.)
[2] Convergence Semiconductor Research Center, Dankook University, Yongin 16890, Korea
* Correspondence: jkang@dankook.ac.kr; Tel.: +82-31-8005-3627

Abstract: In this paper, we demonstrate the enhancement in detection sensitivity of an indirect X-ray detector based on poly(3-hexylthiophene) (P3HT) and fullerene derivatives [6,6]-phenyl-C71-butyric acid methyl ester ($PC_{71}BM$) by adding perovskite quantum dots (PeQDs). The weight ratio of P3HT and $PC_{71}BM$ was fixed at 1:1 (20 mg/mL in chlorobenzene), and different amounts of $FAPbBr_3$ PeQDs of (0–3) mg were added to the P3HT:$PC_{71}BM$ active layer solution. The experimental results show that the detector using P3HT:$PC_{71}BM$:$FAPbBr_3$ PeQDs (1 mg) achieved a sensitivity of 2.10 mA/Gy·cm^2. To further improve the sensitivity, a ligand exchange experiment was performed on the P3HT:$PC_{71}BM$:$FAPbBr_3$ PeQDs (1 mg) detector. Under the condition of 12 h ligand exchange time, the detector with P3HT:$PC_{71}BM$:$FAPbBr_3$ PeQDs (1 mg) showed the highest sensitivity of 2.26 mA/Gy·cm^2, which was increased by 28% compared to the pristine detector with a P3HT:$PC_{71}BM$ active layer.

Keywords: perovskite quantum dots; indirect X-ray detector; ligand exchange

Citation: Lee, K.; Lee, J.; Han, D.; Liu, H.; Kang, J. A Study on Improving the Sensitivity of Indirect X-ray Detectors by Adding Hybrid Perovskite Quantum Dots. *Coatings* **2022**, *12*, 492. https://doi.org/10.3390/coatings12040492

Academic Editor: Ana-Maria Lepadatu

Received: 3 March 2022
Accepted: 4 April 2022
Published: 6 April 2022

1. Introduction

Recently, research has been conducted on the synthesis of various nanocrystals (NCs) that can be applied to optoelectronics and photonic devices [1–4]. The NCs with different structures and dimensions are attracting considerable attention because of their different electrical and optical properties. The structures and dimensions of the NCs can be adjusted as needed, and they are divided into zero-dimensional (0D) quantum dots (QDs) [5,6], one-dimensional (1D) nanorods (NRs) [7], nanowires (NWs) [8], and two-dimensional (2D) nanoplatelets (NPLs) [9,10]. The different structures of NCs have their own advantages. For example, 0D QDs are physically and chemically stable, while 1D NRs are long continuous structures with reduced ligand-induced resistance due to minimizing charge transfer between cores [11]. The 2D NPLs induce a strong quantum confinement effect in one direction to increase quantum efficiency [12]. Among zero-dimensional QDs, ABX_3 (A = Cs, formamidinium (FA), methylammonium (MA), B = Pb, Sn, and X = Cl, Br, I) perovskite quantum dots (PeQDs) have been synthesized under simpler process conditions compared to cadmium-based QDs, and appropriate optical properties can be obtained by tuning the material composition during synthesis [13–18]. PeQDs has a relatively high carrier mobility due to the perovskite crystal structure that promotes charge transport [19] and has excellent optical properties due to its narrow full width at half maximum (FWHM) [20] and high-photoluminescence quantum yield (PLQY) [21]. In addition, compared to the bulk structure, it is suitable for flexible device applications in the same manner as other zero-dimensional QDs [22–24]. Therefore, PeQDs can be applied in various fields, because it is easy to optimize the energy bandgap between materials, and they offer many structural advantages [25,26].

The PeQDs are being applied in various fields, such as displays [27], sensors [28], and memory devices [29]. In addition, bulk-type perovskite materials have the advantages of long carrier diffusion length, low defect density and high carrier mobility, so they are applied to solar cells [30,31], detectors [32,33] and phototransistors [34]. Among these, the X-ray detector is being used as the core of non-destructive testing, and the higher the sensitivity per area, the easier it is to apply, so research in the field is expanding [35–39]. X-ray detectors are divided into two types: direct detection and indirect detection, depending on whether or not a detector is coupled to the scintillator. Direct detection is a method by which X-rays irradiated to a photoconductor layer without a scintillator are directly converted into charges and collected on electrodes. Indirect detection is a method by which a photodetector is coupled with a scintillator, and irradiated X-rays are converted into visible photons by the scintillator, to generate charges in the photodetector active layer. Although the direct detection method has the advantage of high resolution, it introduces design restrictions due to its thick thickness and high voltage. On the other hand, the indirect detection method has low resolution, but it is cheap and can be operated at low voltage, so it is being applied in a relatively wide variety of fields.

In this paper, we fabricated detectors using an organic active layer with added organic–inorganic NCs, composed of electron donor conjugated polymer poly(3-hexylthiophene) (P3HT) and electron acceptor fullerene derivatives [6,6]-phenyl-C71-butyric acid methyl ester ($PC_{71}BM$) with the addition of formamidinium lead trihalide perovskite quantum dots ($FAPbBr_3$ PeQDs) (Qdot^{TM} ABX3-530, Quantum Solutions, Southampton, UK) as active layer. Figure 1a shows a schematic of the proposed detector. In the device structure, poly(3,4-ethylenedioxythiophene):polystyrene sulfonate (PEDOT:PSS) was used as a hole transport layer (HTL) to facilitate hole transport. The P3HT:$PC_{71}BM$ active layer improved the absorbance of the detector by adding $FAPbBr_3$ PeQDs. Figure 1b shows the corresponding energy level and carrier generation–collection process of the proposed detector. The detector without a scintillator operated as a photodetector, and short-circuit current density (J_{SC}) and series resistance (R_S) were extracted from the J−V curve of the photodetector. The electrical properties evaluated without the scintillator could be used to predict the detector performance in advance. The incident visible photons generated by the CsI(TI) scintillator formed excitons in the P3HT:$PC_{71}BM$ active layer and were separated into electrons and holes at the heterojunction. The added $FAPbBr_3$ PeQDs improved detector sensitivity by facilitating visible photon absorption and carrier generation. The amount of charge collected on the electrode could be used to determine the radiation parameters, such as the collected current density (CCD), dark current density (DCD), and sensitivity.

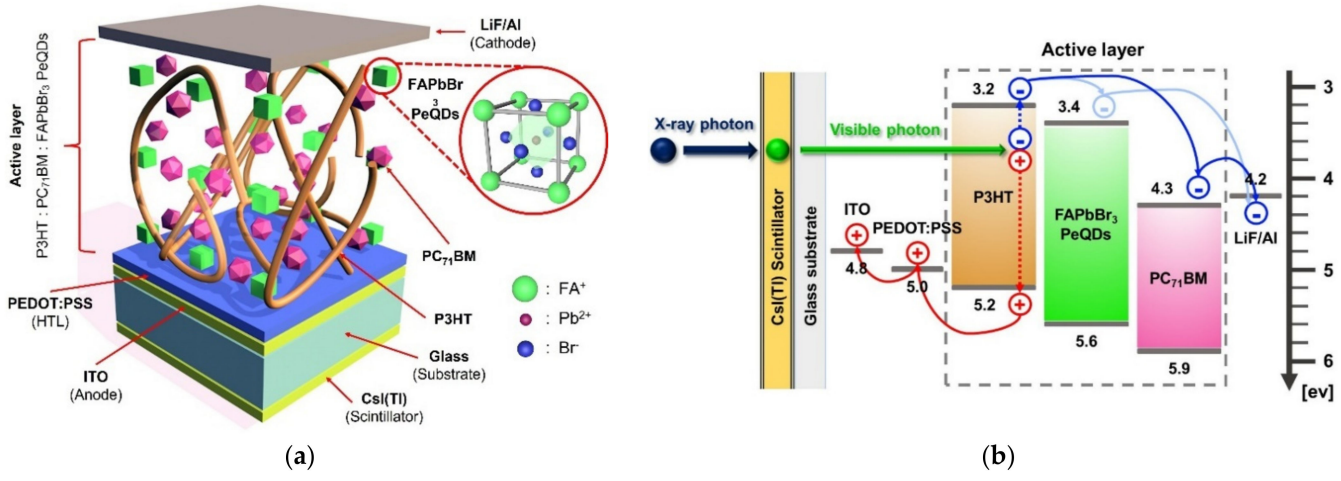

Figure 1. (**a**) Schematic and (**b**) energy band diagram of the X-ray detector with P3HT:$PC_{71}BM$:$FAPbBr_3$ PeQDs.

2. Experimental Detail

2.1. Detector Fabrication Flow

Figure 2 shows the fabrication process of the detector using P3HT:$PC_{71}BM$ active layer added with $FAPbBr_3$ PeQDs. Here, the average size of $FAPbBr_3$ PeQDs was 9.6 nm. First, the indium tin oxide (ITO)-patterned glass was cleaned in an ultrasonic bath, and it was then sequentially treated for 5 min with acetone, methanol, and isopropyl alcohol (IPA). Next, it was baked in a vacuum oven at 100 °C for 10 min, and the glass surface was changed from hydrophobic to hydrophilic by UV treatment for 15 min. To form HTL, PEDOT:PSS blended with dimethylformamide (DMF) at a ratio of 50 wt.% was spin-coated onto the cleaned glass substrate at 3000 rpm for 30 s, and it was baked at 160 °C for 30 min on a hot plate. For the active layer, the mixture of P3HT and $PC_{71}BM$ of weight ratio 1:1 was dissolved in chlorobenzene (20 mg/mL) containing various amounts of $FAPbBr_3$ PeQDs. A solution of $FAPbBr_3$ PeQDs dispersed in toluene was mixed with acetonitrile at a ratio of 5:4 and purified by centrifugation to obtain $FAPbBr_3$ PeQDs powder. The amount of $FAPbBr_3$ PeQDs was measured by analytical balance (AS 82/220.R2, Radwag, Radom, Poland). The $FAPbBr_3$ PeQDs were added in P3HT:$PC_{71}BM$ solution with (0, 1, 2, and 3) mg weight amount, and stirred for 3 h at 60 °C. The P3HT:$PC_{71}BM$:$FAPbBr_3$ active layer solution was spin-coated on the HTL at 700 rpm for 30 s and baked at 120 °C for 10 min. Then the LiF/Al (0.5 nm/120 nm) cathode was deposited on the active layer using a thermal evaporator under a pressure of 10^{-7} torr. Finally, the fabricated detector was sealed with a cover glass in a glove box under nitrogen conditions.

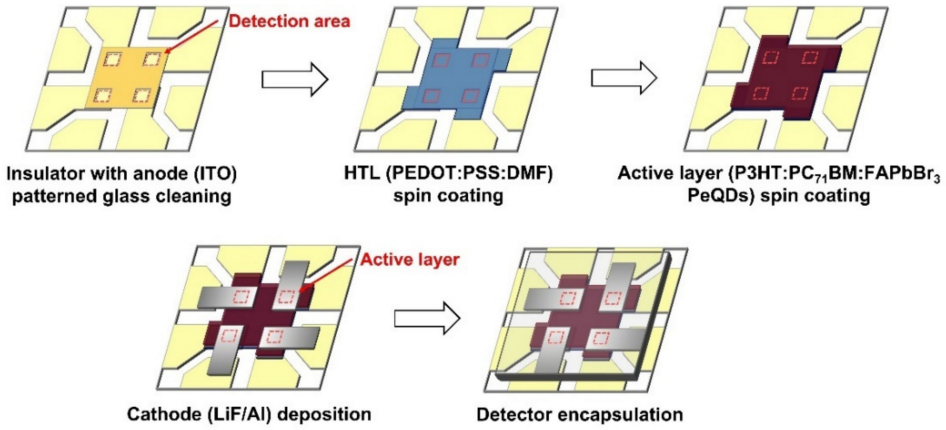

Figure 2. The fabrication flow of the detector with P3HT:$PC_{71}BM$:$FAPbBr_3$ PeQDs.

2.2. Experimental Set-Up

Figure 3 shows the experimental set-up and equipment layout for extracting the characteristics of the detector. The performance evaluation of the detector is performed separately from solar parameter measurement using a solar simulator (XES-40S2-CE, San-Ei Electric, Osaka, Japan) and X-ray parameter measurement using an X-ray generator (AJEX 2000H, AJEX Meditech, Suwon, South Korea). First, the solar parameters, such as J_{SC} and R_S, of the photodetector without the scintillator were evaluated. The photodetector was exposed to a 100 mW/cm^2 xenon lamp filtered with AM 1.5 G, and the J−V characteristics were measured using a source meter (Keithley 2400, Tektronix, Beaverton, OR, USA). By extracting the solar parameters, the characteristics of the photodetector could be analyzed, and the radiation characteristics of the detector combined with photodetector and scintillator could be determined. In the next step, the radiation parameters of the detector were evaluated. The detector combined with scintillator (J13113, Hamamatsu Photonics, Shizuoka, Japan) was placed at a distance of 30 cm from the X-ray generator. The operating conditions of the X-ray generator were fixed at 80 kVp and 60 mAs, and the exposure time was 1.57 s. The charge generated by X-ray exposure was collected by applying a −0.6 V bias voltage between the anode and cathode of the detector. The CCD, which defined when

X-rays were irradiated, and the DCD, which defined when X-rays were not irradiated, were calculated by Equations (1) and (2), respectively:

$$\text{CCD } [\mu A/cm^2] = \text{Collected current during X-ray ON}/\text{Exposed time} \cdot \text{Exposed detector area} \quad (1)$$

$$\text{DCD } [\mu A/cm^2] = \text{Collected current during X-ray OFF}/\text{Exposed time} \cdot \text{Exposed detector area} \quad (2)$$

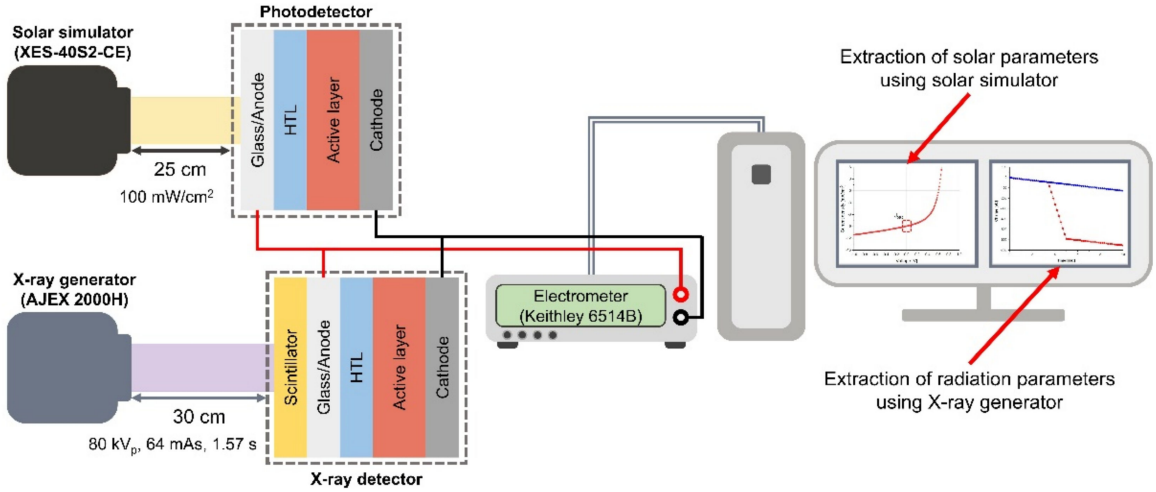

Figure 3. Schematic of the experimental set-up for extracting the photodetector and radiation detector parameters.

At the same time, the absorbed dose was measured by using an ion chamber (Capintec CII50, Mirion Technologies, Florham Park, NJ, USA), and the value was 3.34 mGy. The sensitivity is defined as the rate of charge generated in the absorbed dose, which was calculated by Equation (3):

$$\text{Sensitivity } [mA/Gy \cdot cm^2] = (\text{CCD—DCD})/\text{Absorbed Dose} \quad (3)$$

3. Results and Discussion

3.1. Experiment on P3HT:PC$_{71}$BM Active Layer with Different Amounts of FAPbBr$_3$ PeQDs

Figure 4a shows the absorption spectra of the pristine P3HT:PC$_{71}$BM and P3HT:PC$_{71}$BM with different amounts of FAPbBr$_3$ PeQDs by using UV/Vis spectrophotometry (OPTIZEN 2120UV, Mechasys, Daejeon, Korea). The absorbance of active layers tended to increase as the amount of FAPbBr$_3$ PeQDs added increased within the range of (0–3) mg, and the highest absorbance was observed under the P3HT:PC$_{71}$BM:FAPbBr$_3$ PeQDs (3 mg) film condition due to the high extinction coefficient of FAPbBr$_3$ PeQDs added to the P3HT:PC$_{71}$BM active layer and the absorbance of the P3HT:PC$_{71}$BM:FAPbBr$_3$ PeQDs film being higher than that of the pristine P3HT:PC$_{71}$BM film. In addition, Figure 4a shows the emission peak (560 nm) of the CsI(TI) scintillator that was measured when X-rays were irradiated. Comprehensive results show the absorbance of the P3HT:PC$_{71}$BM:FAPbBr$_3$ PeQDs active layer has a peak similar to the emission peak (560 nm) of the CsI(TI) scintillator. Figure 4b shows the J−V curves of the photodetector based on the P3HT:PC$_{71}$BM active layer with different amounts of FAPbBr$_3$ PeQDs under AM 1.5 G conditions with an intensity of 100 mW/cm^2.

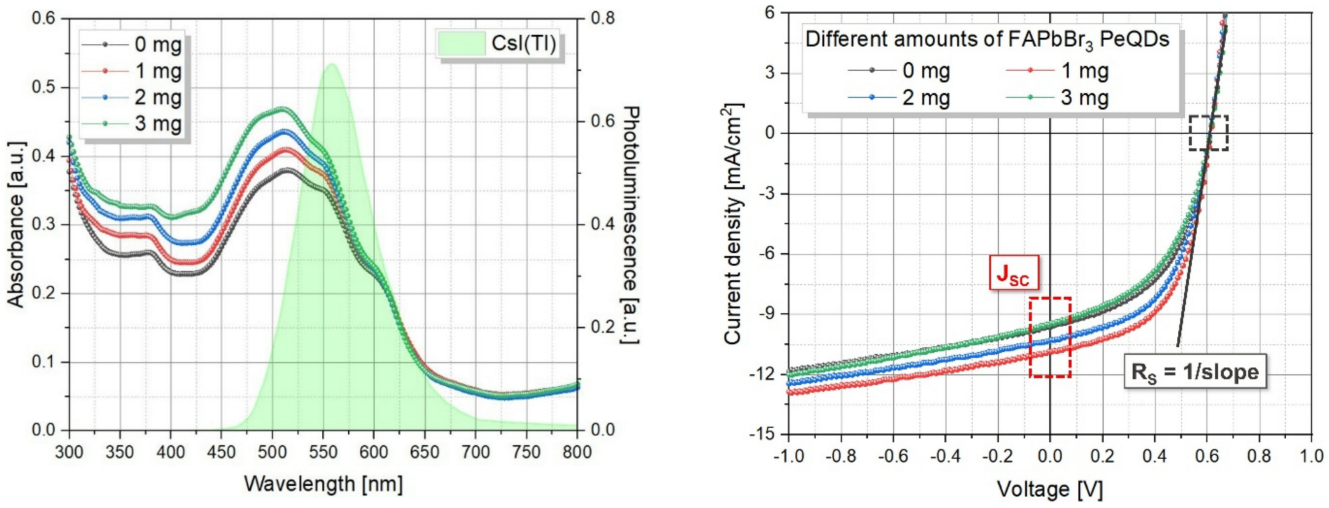

(**a**) (**b**)

Figure 4. (**a**) The absorption spectra of P3HT:PC_{71}BM:$FAPbBr_3$ PeQDs (0, 1, 2, and 3) mg films and the emission spectrum of the CsI(TI) scintillator, (**b**) J−V curves of the detectors based on the P3HT:PC_{71}BM active layer with different amounts of $FAPbBr_3$ PeQDs.

Table 1 lists the measured parameters J_{SC} and R_S. The photodetector based on the pristine P3HT:PC_{71}BM exhibits a J_{SC} of 9.59 mA/cm^2 and R_S of 324.58 Ω. After the incorporation of varying amounts of $FAPbBr_3$ PeQDs, the performance of the detectors with $FAPbBr_3$ additive active layer was improved. This is because the $FAPbBr_3$ PeQDs dispersed in P3HT:PC_{71}BM improve the performance of the detector by increasing photon absorption. The performance of the device with $FAPbBr_3$ PeQDs (1 mg) exhibited a J_{SC} of 11.05 mA/cm^2 and R_S of 262.79 Ω. However, when the amount of $FAPbBr_3$ PeQDs was increased to 3 mg, it was estimated that the performance of the device was significantly reduced, due to the formation of trap sites for charge recombination.

Table 1. The evaluated parameters (J_{SC} and R_S) of the proposed detectors.

PeQDs Amounts [mg]	J_{SC} [mA/cm^2]	R_S [Ω]
0	9.59	324.59
1	11.05	262.79
2	10.46	305.57
3	9.41	349.55

As mentioned in the experimental set-up, the X-ray generator was set up under the same conditions, and the photodetector and CsI(TI) scintillator were combined to measure the amount of charge generated during X-ray irradiation. Regarding the stability upon X-ray exposure, we referred to a study on the stability measurement of P3HT:PC_{61}BM detector [40]. The exposed X-ray dose rate was ~100 mGy/s for 1 h, and a 2.3 % decrease in photocurrent was observed after X-ray exposure. Figure 5a shows the charge density in the X-ray ON state and X-ray OFF state. The X-ray exposure time and measurement distance were fixed at 1.57 s and 30 cm, respectively. Referring to Equations (1)–(3), CCD, DCD, and sensitivity were calculated. Figure 5b shows the radiation parameters (sensitivity and CCD—DCD) of the detectors based on the P3HT:PC_{71}BM and P3HT:PC_{71}BM active layer with different amounts of $FAPbBr_3$ PeQDs. The CCD and sensitivity of the detector based on P3HT:PC_{71}BM:$FAPbBr_3$ PeQDs (1 mg) were improved by 18.64%, as compared to the pristine device based on the pristine P3HT:PC_{71}BM active layer, which is mainly attributed to the synergic enhancement in J_{SC}.

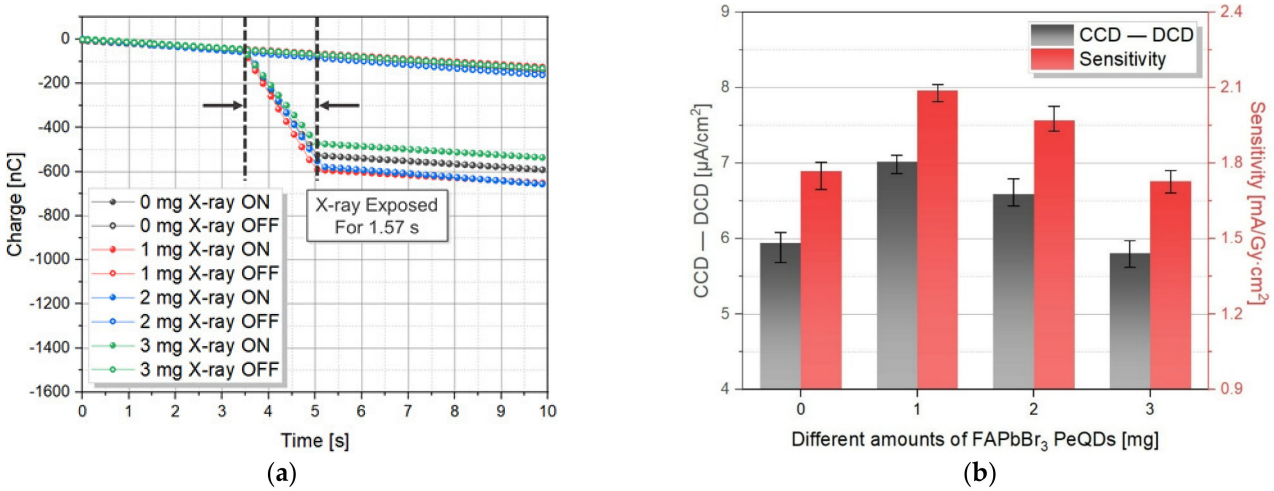

Figure 5. (**a**) C−S characteristic curve, and (**b**) radiation parameters (CCD—DCD and sensitivity) of the detectors based on the P3HT:$PC_{71}BM$ active layer with different amounts of $FAPbBr_3$ PeQDs.

To understand the effect of $FAPbBr_3$ PeQDs incorporation on the morphology of the P3HT:$PC_{71}BM$ films, we used atomic force microscopy (AFM) to measure the morphology of the pristine P3HT:$PC_{71}BM$ and P3HT:$PC_{71}BM$ with different amounts of $FAPbBr_3$ PeQDs films. Figure 6 shows the AFM images of the corresponding samples. Table 2 shows the surface characterization parameters, such as the average surface roughness (R_a) and the roughness peak-to-peak (R_{max}) of P3HT:$PC_{71}BM$ films with different amounts of $FAPbBr_3$ PeQDs. Since $FAPbBr_3$ PeQDs are nanoparticles, the R_a and R_{max} tend to increase in proportion to the amount added. The increase in absorbance of the active layer in Figure 4a was explained by the R_a. As R_a of the P3HT:$PC_{71}BM$ with different amounts of $FAPbBr_3$ PeQDs active layer increases, the absorption area increases, resulting in effective visible-photon absorption. The carriers generated by the additional photon absorption were increased, and the absorbance was improved, compared to the pristine P3HT:$PC_{71}BM$ active layer. However, when the proportion of $FAPbBr_3$ PeQDs increases in the P3HT:$PC_{71}BM$ active layer, they aggregate to form a large structure, interfering with exciton generation and charge transport [38]. As a result, the performance of the P3HT:$PC_{71}BM$:$FAPbBr_3$ PeQDs (2 mg) was lower than that of the P3HT:$PC_{71}BM$:$FAPbBr_3$ PeQDs (1 mg). In the case of the P3HT:$PC_{71}BM$:$FAPbBr_3$ PeQDs (3 mg), the performance was reduced compared to that of the pristine P3HT:$PC_{71}BM$, because it was significantly affected by PeQDs aggregation.

The detectors were characterized under dark conditions to clarify the potential charge transport phenomenon. Figure 7a shows the log J−V curves of the detectors with the pristine P3HT:$PC_{71}BM$ and P3HT:$PC_{71}BM$:$FAPbBr_3$ PeQDs (1 mg). The carrier mobility could be calculated from the space-charge-limited-current model (SCLC) model using the Mott–Gurney law equation [41]:

$$\mu = (8 \cdot J \cdot L^3)/(9 \cdot {V_a}^2 \cdot \varepsilon_o \cdot \varepsilon_r), \quad (4)$$

where μ is the mobility, J is the current density, L is the thickness of the active layer, V_a is the applied voltage, ε_0 (=8.854 × 10^{-14} F/cm^2) is the product of the free-space dielectric constant, and ε_r is the relative permittivity of the active layer. The thickness of the active layer was measured by surface profiler (KLA-Tencor AS-500), and the relative permittivity of the mixture according to the blending ratio of the P3HT:$PC_{71}BM$:$FAPbBr_3$ PeQDs was calculated using the volume ratio and molecular density. As a result, the detector with the P3HT:$PC_{71}BM$:$FAPbBr_3$ PeQDs (1 mg) obtained the highest mobility of 1.41 × 10^{-4} cm^2/V·s, which is improved by 119% compared to the detector with the

pristine P3HT:$PC_{71}BM$. In addition, the defect densities of the detectors were calculated using Equation (5) [42]:

$$\text{Defect density} = 2\varepsilon_o \cdot \varepsilon_r \cdot V_{TFL}/(q \cdot L^2), \quad (5)$$

where V_{TFL} is the trap-filled limit (TFL) voltage from the plots, and q (1.602×10^{-19} C) is the elementary charge of electron. Under the condition of P3HT:$PC_{71}BM$:$FAPbBr_3$ PeQDs (1 mg), the detector showed the lowest defect density of 1.60×10^{16} cm^{-3}.

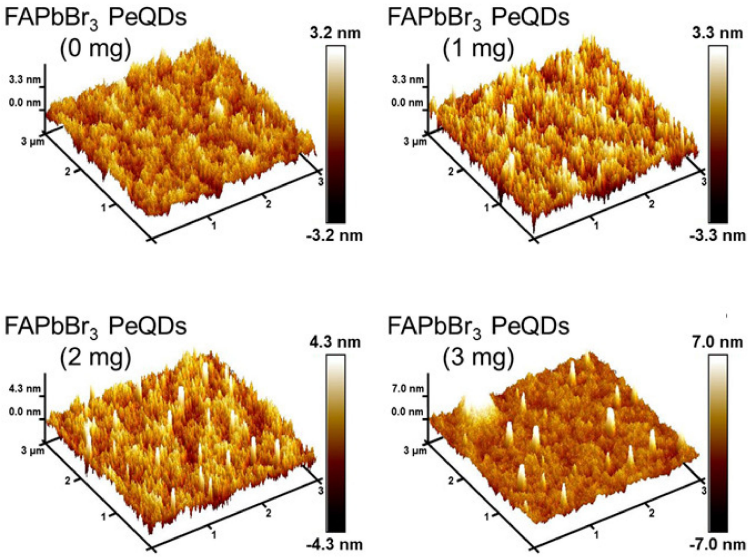

Figure 6. AFM images of the P3HT:$PC_{71}BM$ and P3HT:$PC_{71}BM$:$FAPbBr_3$ PeQDs films.

Table 2. The surface characterization parameters R_a and R_{max} of the corresponding samples.

PeQDs Amounts [mg]	R_a [nm]	R_{max} [nm]
0	0.48	6.6
1	0.62	11.3
2	0.72	14.6
3	0.93	30.2

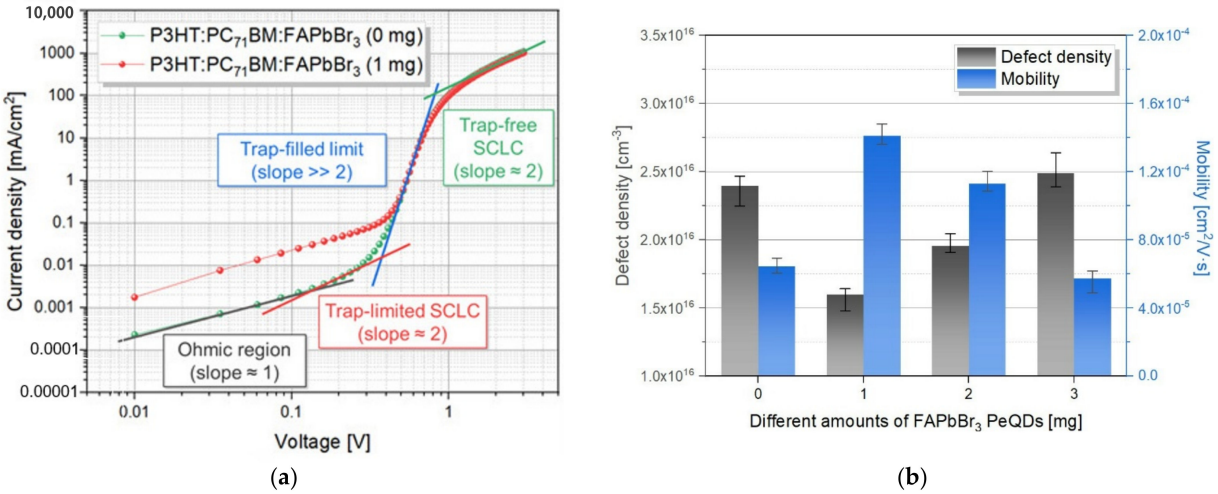

(**a**) (**b**)

Figure 7. (**a**) Log-scale J−V characteristics of the detectors with the pristine P3HT:$PC_{71}BM$ and P3HT:$PC_{71}BM$:$FAPbBr_3$ PeQDs (1 mg), and (**b**) the mobility and defect density of the detectors based on P3HT:$PC_{71}BM$ with different amounts of $FAPbBr_3$ PeQDs.

3.2. Experiments on $FAPbBr_3$ PeQDs Ligand Exchange

To ensure optimal charge transport conditions in the active layer based on the P3HT:PC_{71}BM:$FAPbBr_3$ PeQDs (1 mg), we performed ligand exchange experiments. Although the oleic acid and oleylamine (OA/OAm) ligands can prevent aggregation between cores in solution and remain dispersed, the poor conduction of their long chains interferes with charge transport [43]. Here, the OA/OAm ligands of the $FAPbBr_3$ PeQDs were exchanged with pyridine ligand. That is because pyridine is a short-chain ligand with high conductivity, which improves the charge transport path [44]. At the same time, we also performed experiments to confirm the optimal ratio of ligands by changing the ligand exchange time. Ligand exchange experiments were conducted under conditions of (0, 6, 12, and 18) h, and the active layer was fixed with P3HT:PC_{71}BM:$FAPbBr_3$ PeQDs (1 mg). $FAPbBr_3$ PeQDs-covered OA/OAm ligands were dispersed in toluene and mixed with pyridine in a volume ratio of 5:2, and ligand exchange was performed at 30 °C for 0, 6, 12, and 18 h, respectively. Ligand-exchanged $FAPbBr_3$ PeQDs were mixed with P3HT:PC_{71}BM and fabricated and evaluated as individual devices. For further confirmation of the optimal performance of the detector under the different ligand exchange times, thermogravimetric analysis (TGA) measurement was performed for $FAPbBr_3$ PeQDs with (0 and 12) h ligand exchange time. Figure 8a shows the TGA graphs. The temperature change proceeds from the boiling point of OA (286 °C), OAm (384 °C), and pyridine (116 °C) to 500 °C, and the weight loss of the OA/OAm- and pyridine-capped $FAPbBr_3$ PeQDs continues. The total weight loss of $FAPbBr_3$ PeQDs at 0 h was 44.0%, showing the ligand of OA/OAm. The curve for $FAPbBr_3$ PeQDs for 12 h showed that OA/OAm was exchanged for pyridine. A weight loss of 14.9% occurred from the boiling point of pyridine (116 °C) to an intermediate plateau (316.8 °C), which is the ligand of pyridine. We compared the ligand surface coverage of $FAPbBr_3$ PeQDs using TGA graphs [45]. Under the 12 h condition, the surface coverage of OA/OAm was reduced by 30.5% compared to the 0 h condition, and the surface coverage of pyridine was 80.2% higher than that of OA/OAm. Figure 8b shows the normalized surface coverage:

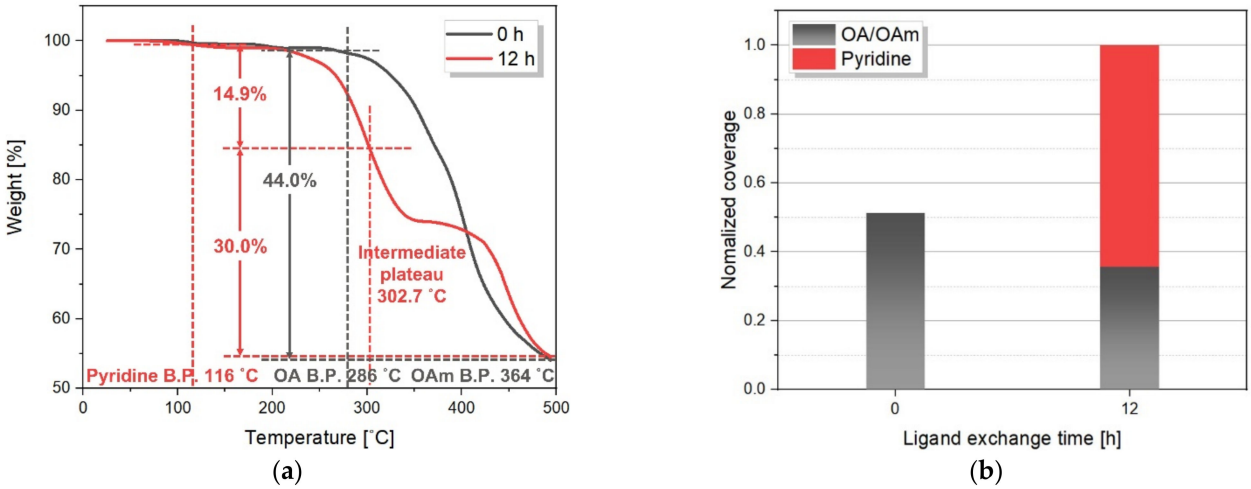

Figure 8. (**a**) The TGA graphs of the (0 and 12) h pyridine ligand exchange time, and (**b**) the normalized coverage ratio (OA/OAm- and pyridine capped) under the (0 and 12) h ligand exchange time.

Figure 9a,b show the evaluation parameters (R_S, mobility, defect density, CCD − DCD, and sensitivity) of the detectors prepared at different exchange times that were obtained. When the ligand exchange time was 12 h, the optimized detector showed the lowest R_S and the highest sensitivity. Compared to the devices with OA/OAm ligands, R_S was 250.05 Ω, which was reduced by 11.01%, and the sensitivity was 2.26 mA/Gy·cm^2, which was increased by 7.84%. However, the radiation properties of the X-ray detector were decreased

under the condition of 18 h, because the large structure of the aggregated $FAPbBr_3$ PeQDs was defective, resulting in increased defect density and R_S and decreased mobility.

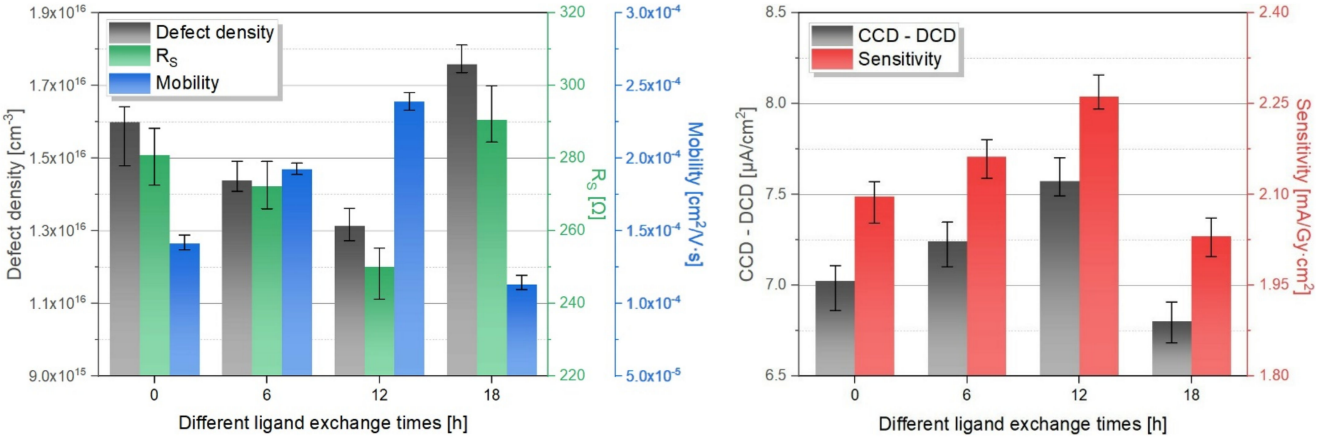

Figure 9. (**a**) The mobility and defect density of the proposed detectors with different pyridine ligand exchange times, and (**b**) the evaluated parameters (R_S, CCD—DCD, and sensitivity) of the detectors based on P3HT:$PC_{71}BM$ active layer with $FAPbBr_3$ PeQDs (1 mg) at (0, 6, 12, and 18) h ligand exchange time.

4. Conclusions

In this paper, we studied the characteristics of an organic X-ray detector in which the active layer is composed of P3HT, $PC_{71}BM$, and $FAPbBr_3$ PeQDs. The performance of the detector was improved by adding $FAPbBr_3$ PeQDs to the P3HT:$PC_{71}BM$ active layer constituting the bulk-heterojunction. First, the amount of $FAPbBr_3$ PeQDs added to the pure P3HT:$PC_{71}BM$ detector was fixed at (0, 1, 2, and 3) mg, and the absorbance of the active layer was measured. As the amount of $FAPbBr_3$ PeQDs increased, the absorbance of the active layer tended to increase linearly. As a result, the sensitivity of the detector based on the P3HT:$PC_{71}BM$:$FAPbBr_3$ PeQDs (1 mg) was 2.10 mA/Gy·cm^2, which was increased by 18.64%. Solar and radiation parameters of the detectors with the P3HT:$PC_{71}BM$:$FAPbBr_3$ PeQDs active layer were optimized by the addition of 1 mg $FAPbBr_3$ PeQDs, compared to the pristine P3HT:$PC_{71}BM$ detector, due to the increased J_{SC} and mobility. Second, to further improve the performance under the conditions of P3HT:$PC_{71}BM$:$FAPbBr_3$ PeQDs (1 mg), an experiment was conducted in which the OA/OAm ligand was replaced by a pyridine ligand. The short-chain ligand pyridine promoted charge transport, compared to the long-chain ligand of OA/OAm. The ligand exchange experiment was conducted under conditions of (0, 6, 12, and 18) h, and the surface coverage ratio of the short-chain ligand was increased to efficiently transport charges. Under the condition of 12 h, the optimized detector showed the highest sensitivity of 2.26 mA/Gy·cm^2, which, compared to the P3HT:$PC_{71}BM$:$FAPbBr_3$ PeQDs (1 mg, 0 h), was increased by 7.84%.

Author Contributions: Conceptualization, J.K.; formal analysis, K.L., J.L., D.H. and J.K.; investigation, K.L., J.L., D.H. and J.K.; data curation, K.L., J.L, D.H. and J.K.; writing—original draft preparation, K.L., J.L. and J.K.; writing—review and editing, K.L., J.L., H.L. and J.K.; visualization, K.L., J.L. and J.K.; supervision, J.K.; project administration, J.K.; funding acquisition, J.K. All authors have read and agreed to the published version of the manuscript.

Funding: This research was supported by National R&D Program through the National Research Foundation of Korea (NRF) funded by the Ministry of Science and ICT (2021M3H2A1038042).

Institutional Review Board Statement: Not applicable.

Informed Consent Statement: Not applicable.

Data Availability Statement: Data is contained within the article.

Conflicts of Interest: The authors declare no conflict of interest.

References

1. Chen, L.C.; Tien, C.H.; Tseng, P.W.; Tseng, Z.L.; Huang, W.L.; Xu, Y.X.; Kuo, H.C. Effect of Washing Solvents on the Properties of Air-Synthesized Perovskite $CsPbBr_3$ Quantum Dots for Quantum Dot-Based Light-Emitting Devices. *IEEE Access* **2020**, *8*, 159415–159423. [CrossRef]
2. Shekhirev, M.; Goza, J.; Teeter, J.; Lipatov, A.; Sinitskii, A. Synthesis of Cesium Lead Halide Perovskite Quantum Dots. *J. Chem. Educ.* **2017**, *94*, 1150–1156. [CrossRef]
3. Ithurria, S.; Bousquet, G.; Dubertret, B. Continuous Transition from 3D to 1D Confinement Observed during the Formation of CdSe Nanoplatelets. *J. Am. Chem. Soc.* **2011**, *133*, 3070–3077. [CrossRef] [PubMed]
4. Lupan, O.; Emelchenko, G.A.; Ursaki, V.V.; Chai, G.; Redkin, A.N.; Gruzintsev, A.N.; Tiginyanu, I.M.; Chow, L.; Ono, L.K.; Roldan Cuenya, B.; et al. Synthesis and characterization of ZnO nanowires for nanosensor applications. *Mater. Res. Bull.* **2010**, *45*, 1026–1032. [CrossRef]
5. Neeleshwar, S.; Chen, C.L.; Tsai, C.B.; Chen, Y.Y.; Chen, C.C.; Shyu, S.G.; Seehra, M.S. Size-dependent properties of CdSe quantum dots. *Phys. Rev. B* **2005**, *71*, 201307. [CrossRef]
6. Kim, B.; Lee, J.; Kang, J. Improving the sensitivity of indirect-type organic X-ray detector by blending with CdSe quantum dots. *J. Instrum.* **2017**, *12*, C01009. [CrossRef]
7. Yi, G.; Wang, C.; Park, W. ZnO nanorods: Synthesis, characterization and applications. *Semicond. Sci. Technol.* **2005**, *20*, S22–S34. [CrossRef]
8. Yang, P.; Yan, H.; Mao, S.; Russo, R.; Johnson, J.; Saykally, R.; Morris, N.; Pham, J.; He, R.; Choi, H.-J. Controlled Growth of ZnO Nanowires and Their Optical Properties. *Adv. Funct. Mater.* **2002**, *12*, 323–331. [CrossRef]
9. Ghosh, G.; Dutta, A.; Ghosh, A.; Ghosh, S.; Patra, A. Ultrafast Carrier Dynamics in 2D CdSe Nanoplatelets–$CsPbX_3$ Composites: Influence of the Halide Composition. *J. Phys. Chem. C* **2020**, *124*, 10252–10260. [CrossRef]
10. Pedetti, S.; Ithurria, S.; Heuclin, H.; Patriarche, G.; Dubertret, B. Type-II CdSe/CdTe Core/Crown Semiconductor Nanoplatelets. *J. Am. Chem. Soc.* **2014**, *136*, 16430–16438. [CrossRef]
11. Gao, Y.; Cao, D.; Liu, J.; Shen, J.; Wu, Y.; Zhang, L. Molecular dynamics simulation of the conductivity mechanism of nanorod filled polymer nanocomposites. *Phys. Chem. Chem. Phys.* **2015**, *17*, 22959–22968. [CrossRef] [PubMed]
12. Yu, J.; Chen, R. Optical properties and applications of two-dimensional CdSe nanoplatelets. *InfoMat* **2020**, *2*, 905–927. [CrossRef]
13. Choi, J.W.; Woo, H.C.; Huang, X.; Jung, W.G.; Kim, B.J.; Jeon, S.W.; Yim, S.Y.; Lee, J.S.; Lee, C.L. Organic–inorganic hybrid perovskite quantum dots with high PLQY and enhanced carrier mobility through crystallinity control by solvent engineering and solid-state ligand exchange. *Nanoscale* **2018**, *10*, 13356–13367. [CrossRef] [PubMed]
14. Ye, S.; Zhao, M.; Song, J.; Qu, J. Controllable emission bands and morphologies of high-quality $CsPbX_3$ perovskite nanocrystals prepared in octane. *Nano Res.* **2018**, *11*, 4654–4663. [CrossRef]
15. Yan, A.; Guo, Y.; Liu, C.; Deng, Z.; Guo, Y.; Zhao, X. Tuning the Optical Properties of $CsPbBr_3$ Nanocrystals by Anion Exchange Reactions with CsX Aqueous Solution. *Nanoscale Res. Lett.* **2018**, *13*, 1–7. [CrossRef]
16. Liu, S.; He, M.; Di, X.; Li, P.; Xiang, W.; Liang, X. Precipitation and tunable emission of cesium lead halide perovskites ($CsPbX_3$, X = Br, I) QDs in borosilicate glass. *Ceram. Int.* **2018**, *44*, 4496–4499. [CrossRef]
17. Li, G.; Wang, H.; Zhang, T.; Mi, L.; Zhang, Y.; Zhang, Z.; Zhang, W.; Jiang, Y. Solvent-Polarity-Engineered Controllable Synthesis of Highly Fluorescent Cesium Lead Halide Perovskite Quantum Dots and Their Use in White Light-Emitting Diodes. *Adv. Funct. Mater.* **2016**, *26*, 8478–8486. [CrossRef]
18. Minh, D.N.; Kim, J.; Hyon, J.; Sim, J.H.; Sowlih, H.H.; Seo, C.; Nam, J.; Eom, S.; Suk, S.; Lee, S.; et al. Room-Temperature Synthesis of Widely Tunable Formamidinium Lead Halide Perovskite Nanocrystals. *Chem. Mater.* **2017**, *29*, 5713–5719. [CrossRef]
19. Liang, J.; Chen, D.; Yao, X.; Zhang, K.; Qu, F.; Qin, L.; Huang, Y.; Li, J. Recent Progress and Development in Inorganic Halide Perovskite Quantum Dots for Photoelectrochemical Applications. *Small* **2020**, *16*, 1903398. [CrossRef]
20. Protesescu, L.; Yakunin, S.; Bodnarchuk, M.I.; Krieg, F.; Caputo, R.; Hendon, C.H.; Yang, R.X.; Walsh, A.; Kovalenko, M.V. Nanocrystals of Cesium Lead Halide Perovskites ($CsPbX_3$, X = Cl, Br, and I): Novel Optoelectronic Materials Showing Bright Emission with Wide Color Gamut. *Nano Lett.* **2015**, *15*, 3692–3696. [CrossRef]
21. Dai, S.W.; Hsu, B.W.; Chen, C.Y.; Lee, C.A.; Liu, H.Y.; Wang, H.F.; Huang, Y.C.; Wu, T.L.; Manikandan, A.; Ho, R.M.; et al. Perovskite Quantum Dots with Near Unity Solution and Neat-Film Photoluminescent Quantum Yield by Novel Spray Synthesis. *Adv. Mater.* **2018**, *30*, 1705532. [CrossRef] [PubMed]
22. Liu, J.; Shabbir, B.; Wang, C.; Wan, T.; Ou, Q.; Yu, P.; Tadich, A.; Jiao, X.; Chu, D.; Qi, D.; et al. Flexible, Printable Soft-X-Ray Detectors Based on All-Inorganic Perovskite Quantum Dots. *Adv. Mater.* **2019**, *31*, 1901644. [CrossRef] [PubMed]
23. Zhao, F.; Chen, D.; Chang, S.; Huang, H.; Tong, K.; Xiao, C.; Chou, S.; Zhong, H.; Pei, Q. Highly flexible organometal halide perovskite quantum dot based light-emitting diodes on a silver nanowire–polymer composite electrode. *J. Mater. Chem. C* **2017**, *5*, 531–538. [CrossRef]
24. Li, Y.; Lv, Y.; Guo, Z.; Dong, L.; Zheng, J.; Chai, C.; Chen, N.; Lu, Y.; Chen, C. One-Step Preparation of Long-Term Stable and Flexible $CsPbBr_3$ Perovskite Quantum Dots/Ethylene Vinyl Acetate Copolymer Composite Films for White Light-Emitting Diodes. *ACS Appl. Mater. Interfaces* **2018**, *10*, 15888–15894. [CrossRef] [PubMed]

25. Wei, Y.; Cheng, Z.; Lin, J. An overview on enhancing the stability of lead halide perovskite quantum dots and their applications in phosphor-converted LEDs. *Chem. Soc. Rev.* **2019**, *48*, 310–350. [CrossRef] [PubMed]
26. Mali, S.S.; Shim, C.S.; Hong, C.K. Highly stable and efficient solid-state solar cells based on methylammonium lead bromide ($CH_3NH_3PbBr_3$) perovskite quantum dots. *NPG Asia Mater.* **2015**, *7*, e208. [CrossRef]
27. Lin, J.; Lu, Y.; Li, X.; Huang, F.; Yang, C.; Liu, M.; Jiang, N.; Chen, D. Perovskite quantum dots glasses based backlit displays. *ACS Energy Lett.* **2021**, *6*, 519–528. [CrossRef]
28. Huang, S.; Guo, M.; Tan, J.; Geng, Y.; Wu, J.; Tang, Y.; Su, C.; Lin, C.C.; Liang, Y. Novel fluorescence sensor based on all-inorganic perovskite quantum dots coated with molecularly imprinted polymers for highly selective and sensitive detection of omethoate. *ACS Appl. Mater. Interfaces* **2018**, *10*, 39056–39063. [CrossRef]
29. Li, Q.; Li, T.; Zhang, Y.; Yu, Y.; Chen, Z.; Jin, L.; Li, Y.; Yang, Y.; Zhao, H.; Li, J.; et al. Nonvolatile photoelectric memory with CsPbBr3 quantum dots embedded in poly (methyl methacrylate) as charge trapping layer. *Org. Electron.* **2020**, *77*, 105461. [CrossRef]
30. Lin, Y.; Li, T.; Liu, Y.; Bahrami, B.; Guo, D.; Fang, Y.; Shao, Y.; Chowdhury, A.H.; Wang, Q.; Deng, Y.; et al. Perovskite solar cells with embedded homojunction via nonuniform metal ion doping. *Cell Rep.* **2021**, *2*, 100415.
31. Zhang, G.; Zheng, Y.; Shi, Y.; Ma, X.; Sun, M.; Li, T.; Yang, B.; Shao, Y. Improving the Performance of Perovskite Solar Cells with Insulating Additive-Modified Hole Transport Layers. *ACS Appl. Mater. Interfaces* **2022**, *14*, 11500–11508. [CrossRef] [PubMed]
32. Feng, Y.; Pan, L.; Wei, H.; Liu, Y.; Ni, Z.; Zhao, J.; Rudd, P.N.; Cao, L.R.; Huang, J. Low defects density CsPbBr 3 single crystals grown by an additive assisted method for gamma-ray detection. *J. Mater. Chem. C* **2020**, *8*, 11360–11368. [CrossRef]
33. Pan, L.; Feng, Y.; Kandlakunta, P.; Huang, J.; Cao, L.R. Performance of perovskite CsPbBr3 single crystal detector for gamma-ray detection. *IEEE Trans. Nucl. Sci.* **2020**, *67*, 443–449. [CrossRef]
34. Shao, Y.; Liu, Y.; Chen, X.; Chen, C.; Sarpkaya, I.; Chen, Z.; Fang, Y.; Kong, J.; Watanabe, K.; Taniguchi, T.; et al. Stable graphene-two-dimensional multiphase perovskite heterostructure phototransistors with high gain. *Nano Lett.* **2017**, *17*, 7330–7338. [CrossRef]
35. Hanke, R.; Fuchs, T.; Uhlmann, N. X-ray based methods for non-destructive testing and material characterization. *Nucl. Instrum. Methods Phys. Res. A* **2008**, *591*, 14–18. [CrossRef]
36. Nagarkar, V.V.; Gordon, J.S.; Vasile, S.; Gothoskar, P.; Hopkins, F. High resolution X-ray sensor for non-destructive evaluation. *IEEE Trans. Nucl. Sci.* **1996**, *43*, 1559–1563. [CrossRef]
37. Chen, P.; Sun, Z. A review of non-destructive methods for quality evaluation and sorting of agricultural products. *J. Agric. Eng. Res.* **1991**, *49*, 85–98. [CrossRef]
38. Kim, S.; Lee, J.; Kang, J. Sensitivity Improvement of Quantum Dot-Blended Hybrid Detector for X-ray Imaging. *Coatings* **2020**, *10*, 222. [CrossRef]
39. Lee, J.; Liu, H.; Kang, J. A Study on an Organic Semiconductor-Based Indirect X-ray Detector with Cd-Free QDs for Sensitivity Improvement. *Sensors* **2020**, *20*, 6562. [CrossRef]
40. Kingsley, J.W.; Pearson, A.J.; Harris, L.; Weston, S.J.; Lidzey, D.G. Detecting 6 MV X-rays using an organic photovoltaic device. *Org. Electron.* **2009**, *10*, 1170–1173. [CrossRef]
41. Murgatroyd, P.N. Theory of space-charge-limited current enhanced by Frenkel effect. *J. Phys. D* **1970**, *3*, 151. [CrossRef]
42. Shi, J.; Jin, X.; Wu, Y.; Shao, M. Mixed bulky cations for efficient and stable Ruddlesden—Popper perovskite solar cells. *APL Mater.* **2020**, *8*, 101102. [CrossRef]
43. Bi, C.; Kershaw, S.V.; Rogach, A.L.; Tian, J. Improved Stability and Photodetector Performance of $CsPbI_3$ Perovskite Quantum Dots by Ligand Exchange with Aminoethanethiol. *Adv. Funct. Mater.* **2019**, *29*, 1902446. [CrossRef]
44. Lokteva, I.; Radychev, N.; Witt, F.; Borchert, H.; Parisi, J.; Kolny-Olesiak, J. Surface Treatment of CdSe Nanoparticles for Application in Hybrid Solar Cells: The Effect of Multiple Ligand Exchange with Pyridine. *J. Phys. Chem. C* **2010**, *114*, 12784–12791. [CrossRef]
45. Kuno, M.; Lee, J.K.; Dabbousi, B.O.; Mikulec, F.V.; Bawendi, M.G. The band edge luminescence of surface modified CdSe nanocrystallites: Probing the luminescing state. *J. Chem. Phys.* **1997**, *106*, 9869–9882. [CrossRef]